C$_2$N-Supported Single Metal Ion Catalyst for HCOOH Dehydrogenation

C$_2$N-Supported Single Metal Ion Catalyst for HCOOH Dehydrogenation

Wenhui Zhong,[1] Yuxia Liu,[2] Mingsen Deng,[1] Yachao Zhang,[1] Chuanyi Jia,[1] Oleg V. Prezhdo,[3] Jianyong Yuan,[4] and Jun Jiang[5,*]

[1]Guizhou Provincial Key Laboratory of Computational Nano-Material Science, Institute of Applied Physics, Guizhou Synergetic Innovation Center of Scientific Big Data for Advanced Manufacturing Technology, Guizhou Education University, Gaoxin Road 115, Guiyang, Guizhou 550018, P. R. China;

[2]School of Chemistry and Chemical Engineering, Qufu Normal University, Qufu 273165, P.R. China;

[3]Department of Chemistry, University of Southern California, Los Angeles, California 90089, United States;

[4]Key Laboratory for Ultrafine Materials of Ministry of Education and Shanghai Key Laboratory of Advanced Polymeric Materials, School of Materials Science and Engineering, East China University of Science and Technology, Shanghai 200237, China;

[5]Hefei National Laboratory for Physical Sciences at the Microscale, iChEM (Collaborative Innovation Center of Chemistry for Energy Materials), CAS Center for Excellence in Nanoscience, School of Chemistry and Materials Science, University of Science and Technology of China, Hefei, Anhui 230026, China

*Email: jiangj1@ustc.edu.cn

Abstract

High catalytic performance of a single-atom transition metal ion (TM^{x+}) anchored on the two-dimensional (2D) C_2N lattice is predicted for HCOOH dehydrogenation. Considering the Co^{2+}, Cu^{2+} and Ni^{2+} non-noble metal ions supported by C_2N, we use density functional theory to demonstrate dehydrogenation energy barriers as low as those for pure Pt and Pd catalysts. The high catalytic performance is ascribed to reaction occurring through a dual-active center composed of TM^{x+} and a nearby N atom of C_2N. Specifically, $C_2N–Co^{2+}$ in the low spin state (S = 1/2) greatly promotes HCOOH dehydrogenation by decreasing the barrier of the rate-determining step to only 0.30 eV, mainly due to the strong ability of TM^{x+} in extracting charges from HCOOH and C_2N. The obtained mechanistic insights help the rational design of single-atom based transition metal ion catalysts supported by 2D materials.

1. Introduction

Direct formic acid fuel cell (DFAFC) plays a significant role in sustainable technology development, owing to advantages of high energy density, low toxicity, and small crossover flux through Nafion membranes.[1–3] Pt- and Pd-based catalysts were widely used as DFAFC anodes which exhibited high catalytical performance in driving HCOOH oxidation,[4–8] while their practical applications are limited by the scarcity of precious metals. On the other hand, the utilizations of non-noble transition metals (TMs), such as Co, Ni, Cu, were hindered by very low catalytical activity for HCOOH oxidation.[9–11]

Recently, it was found that using metals or metal oxides as substrate to support single-atom based non-noble TMs can significantly enhance the catalytic activities,[12-14] but practical applications are limited by the high cost of substrate. Therefore, the most promising substrate could be metal free materials, especially carbon-based two-dimensional (2D) materials due to excellent charge delivery ability and structural flexibility. The 2D graphitic carbon-nitrogen (C–N) materials[15,16], breaking a graphene into fragments connected by nitrogen nodes, are good candidate for anchoring TM atoms. For instance, a novel C_2N material, the 2D layered C–N crystal with uniform hole vacancies, is recently prepared through wet chemical reaction and exhibits high electric conductivity.[17] Importantly, its nitrogen nodes could collect polarized charges, and thereby offer chemically active sites for both reactions and anchoring TM atoms. As shown in Figure 1a, its uniform hole structure provides ideal support for TM atoms to bonding chemically with nitrogen, and high

surface-to-volume ratio property ensures sufficient exposure of TM sites to adsorb and catalyze reactive molecules.[18]

Now that single-atom based TM catalysts have exhibited high activity and selectivity in a variety of reactions,[19–22] it becomes a pressing issue to solve the problem of low stability due to TM atom drifting and aggregating. Our recent work[23] revealed the good stability and catalytic O_2 activity of double-atom based TM catalysts (Co–Co, Ni–Ni, and Cu–Cu) on C_2N, owing to the double–bonding feature of N–TM–TM–N structure and the accumulation of polarized charges. Meanwhile, Willner. et al. experimentally reported that Cu^{2+}-ion-modified graphene oxide and carbon nitride nanoparticles showed superior catalytic effect on chemiluminescence reaction.[24,25] As we have also revealed in both simulations and experiments the same effect of Co^{2+} – ion on oxidized graphene for luminol – H_2O_2 chemiluminescence.[26] In addition, Nie et al. recently demonstrated atomically dispersed Pt^{2+} on ceria can simultaneously achieve the goals of low-temperature CO oxidation activity while providing outstanding hydrothermal stability.[27] More importantly, Bulushev et al. experimentally found that N-doped carbon supported single Pd^{2+} cations are active sites for hydrogen production from HCOOH decomposition.[28] So we realized that the design of TM^{x+} ion on C–N substrate can naturally prohibit TM-aggregating due to repulsions between TM-ions and enhance the catalytic activity by extracting polarized charges from reactive molecules and C–N substrate. Here in this work, we applied density functional theory (DFT) calculations to simulate systems of three types of TM^{x+} ions (Co^{2+}, Ni^{2+}, Cu^{2+}) anchoring on C_2N monolayer, based on which the

catalytic activity of HCOOH dehydrogenation was examined. And we expected to design novel C_2N-supported single-atom based TM^{x+} ion catalysts combining advantages of high activity, low cost, and good stability.

2. Computational Details

Theoretical calculations were performed at the Perdew-Burke-Ernzerhof (PBE) exchange functional level of density functional theory (DFT), [29,30] which has been widely used for N-doped carbon supported TM catalyzed systems.[23,31,32] The 6–31G(d, p) basis set[33] and Lanl2DZ[34] were chosen for C, N, H atoms and TM atoms, respectively. Vibration frequency calculations verified that all optimized geometries have no imaginary frequency while every transition state holds only a single imaginary frequency. Calculations of intrinsic reaction coordinates (IRC)[35,36] confirmed that structures of transition states indeed connect two relevant minima. Electron density and partial density-of-states (DOS) were generated with the Multiwfn 3.3.9 program[37], and charge numbers were taken from natural population analysis (NPA).[38,39] Gibbs free energies were computed and used to analyze the reaction mechanism. The binding energy of metal to C_2N ($E_{b-TM^{x+}}$) or adsorption energy of molecule to catalysts were calculated by subtracting the summation energy of isolated molecules/clusters from the total energy of their hybrid system. All calculations were performed with the Gaussian 09 software package.[40] The unit cell of a C_2N lattice contains 12 C and 6 N atoms, and four unit cells form a uniform hole vacancy (Figure 1a). The optimized lattice parameter is 8.32 Å, matching well with experimental result (8.30 Å).[12] To model the interactions with reactants and

intermediates, here we take a ring-alike molecular cluster containing one hole vacancy (Figure 1b), where carbons at the edge of the cluster are saturated with hydrogen terminations.

3. Results and Discussion

We first simulated the deposition of a single TM^{x+} ion (Co^{2+}, Ni^{2+}, Cu^{2+}) onto the small C_2N model cluster (Figure S1). The formation of such C_2N–TM^{x+} systems is quite stable due to the strong bindings between the TM ion and two N atoms with bond lengths of 1.99 ~ 2.18 Å (Figure 1c). The computed binding energies of Co^{2+}, Ni^{2+}, Cu^{2+} anchoring on C_2N are all larger than 14 eV (Table 1), suggesting very strong couplings. It is found that the diffusion barrier from one adsorption position to a neighboring one along the vacancy circle is only 0.07 eV, indicating that ion drifting along the vacancy circle is easy. However, the diffusion barrier is up to 3.91 eV from one hole site to the neighboring hole site[23], demonstrating that strong interaction between TM^{x+} and nitrogen prevents the TM^{x+} aggregation. It is noted that the spin of C_2N–Co^{2+} could be either 1/2 or 3/2 with an energy difference of 0.39 eV, which can be controlled to interconvert by applying external stimuli such as thermal, photochemical, electrochemical, and chemical control of phase transitions.[41,42] In contrast, the binding energy of a neutral Co atom to C_2N is 3.09 and 2.67 eV at S = 1/2 and 3/2, respectively, which are much lower than those of Co^{2+} ion (15.16 and 14.34 eV). Because of strong couplings, electron density difference analysis (EDD) in Figure 1d-g reveals that there are effective electrons transferring from C_2N to TM^{x+}, when the coordination numbers of those three ions are 2 with N atoms of C_2N. The

NPA for charge distribution shows that TM^{x+} ions extract 0.96 ~ 1.12 e^- charges from

C_2N (Table 1). In addition, electronic structures reflected by partial density of states

(PDOS) show that electronic coupling mainly exists between TM^{x+}-3d and N-2p

orbitals (Figure S4).

We then simulated the most stable adsorption state of HCOOH on $C_2N–TM^{x+}$, so

as to explore possible reaction pathways of dehydrogenation. As in Figure 1h,

HCOOH binds to the $C_2N–TM^{x+}$ hybrid through two sites: the carbonyl O locates at

the TM^{x+} ion atop site, and the H of OH group forms hydrogen bond with a N atom of

C_2N near but not connected to the TM^{x+}. The HCOOH adsorption energy of 0.48 ~

1.15 eV suggests strong chemical bondings (Table 1), with the order of $C_2N–Ni^{2+}$ >

$C_2N–Co^{2+}$ > $C_2N–Cu^{2+}$ ~ $C_2N–Co$. Upon adsorption, the O–H bond length is

elongated from 0.98 Å in free HCOOH to 1.17 ~ 1.34 Å if binding with $C_2N–TM^{x+}$.

The adsorption energy of HCOOH on $C_2N–Co$ is 0.49 and 0.58 eV for spin states S =

1/2 and 3/2, respectively, which are weaker than those of $C_2N–Co^{2+}$ (0.83 and 0.84

eV). Additionally, EDD analysis (Figure 1i and S3) reveals effective charges

accumulated at two binding sties of N and TM^{x+}, implying that HCOOH molecule

may react with $C_2N–TM^{x+}$ via these two active sites.

On account of $C_2N–Co^{2+}$ having two spin states, we started with the investigation

of HCOOH dehydrogenation by $C_2N–Co^{2+}$ of S = 1/2. Figure 2 shows the calculated

potential energy profile for HCOOH dehydrogenation on $C_2N–Co^{2+}$ (S = 1/2) with the

optimized geometries of intermediates and transition states involved in the reaction.

Once HCOOH adsorbs on $C_2N–Co^{2+}$ (S = 1/2), the abstraction of H occurs via

transition state TS_{1-2} with no barrier, where the breaking O–H bond is stretched from

1.05 to 1.27 Å. This process is endothermic by 0.04 eV. Notably, before the zero-point

energy (ZPE) correction, TS_{1-2} is computed to be higher by 0.03 eV in intermediate 2.

However, it is 0.04 eV more stable than intermediate 2 after the ZPE correction is

introduced. Note that the harmonic approximation can cause some errors in the ZPE

calculation.[43] The dissociated H atom would locate at the N atop position via N–H

bond with bond length of 1.07 Å, and the newly formed HCOO binds to the surface

via Co–O and O–H hydrogen bonds. Then, intermediate 2 is converted to intermediate

3 via a transition state corresponding to O–H hydrogen bond scission, TS_{2-3}, with a

barrier of 0.1 eV. In intermediate 3, HCOO binds to the bridge site through O–Co and

O–H hydrogen bonds. That process is endothermic by 0.05 eV. Subsequently, the

abstraction of the second H atom occurs through transition state TS_{3-4} with a barrier

of 0.3 eV and a corresponding energy change of 0.14 eV (endothermic reaction step).

This is the rate-determining step of the overall reaction illustrated in Figure 2. As the

H atom is abstracted, the CO_2 binds to the surface via O–Co and O–H hydrogen bonds.

In the final state 4, the newly formed CO_2 weakly adsorbs on the surface via O–H

hydrogen bond with the distance of 2.61 Å and the H atom locates at the atop position

via Co–H bond. Meanwhile, the desorption of CO_2 is exothermic by 0.23 eV (Table 2).

Therefore, the overall dehydrogenation reaction takes place through the O–H bond

scission occurring at the N active site, and the C–H bond scission proceeding through

the Co^{2+} (S = 1/2) active site. Such a dual-active center normally means synergetic

mechanism leading to high catalytic performance.[44] From the energy point of view,

the barrier of the rate-determining step of HCOOH dehydrogenation on C_2N–Co^{2+} (S = 1/2) is 0.30 eV, which is much lower than those of noble Pt or Pd catalysts (0.65 ~ 0.88 eV).[45–47] In addition, the overall reaction is isoenergetic, and the final CO_2 product can desorb easily from the catalyst surface. The H atom formed in DFAFC is easily converted to H_2O and e^- with OH^- assistance during the oxygen reduction reaction on the cathode. The reaction is thus thermodynamically feasible. Here the Polarizable Continuun Model (PCM) is applied to consider the solvent effect[48] and found that the rate-determining step of the overall reaction changed little, characterized by the barrier of 0.42 eV, which is comparable with the gas phase barrier of 0.30 eV. Therefore, solvent has a minor effect on the reaction.

We then move further to study reaction with C_2N–Co^{2+} of high spin of S = 3/2, for which the process is similar to that of S = 1/2. First, the O–H bond scission of HCOOH occurs through transition state TS_{6-7} with no barrier and the step is exothermic by 0.30 eV (Figure S5). It should be noted that the formed HCOO adsorbs on the surface via two Co–O bonds and one O–H hydrogen bond. Then, HCOO twists via transition state TS_{6-7} with a barrier of 0.51eV, and it locates at the bridge site through Co–O and O–H hydrogen bonds. The reaction energy is 0.46 eV (endothermic). Finally, the C–H bond scission proceeds via transition state TS_{7-8} with a barrier of 1.05 eV and a corresponding energy change of 0.68 eV (endothermic reaction step), indicating the second H abstraction is very difficult. This thus means a high barrier for the rate-determining step of the overall reaction (Figure S5). The newly formed CO_2 also weakly binds to the surface via O–H hydrogen bond, and the

H atom locates at the atop position via Co–H bond. The CO_2 desorption is exothermic by 0.54 eV (Table 2).

Clearly, the barrier of the rate-determining step of HCOOH dehydrogenation on $C_2N–Co^{2+}$ (S = 1/2) is lower by 0.75 eV than that on $C_2N–Co^{2+}$ (S = 3/2), meaning that the former is kinetically much more favored than the latter. The former is also thermodynamically more favorable due to less endothermic energy (0.00 vs 0.30 eV). Based on the NPA analysis for charge distribution (Table 1), it is found that Co^{2+} (S = 1/2) can extract 0.07 e^- electrons from the HCOOH molecule to promote the oxidation reaction, which is higher than that of Co^{2+} (S = 3/2, 0.04 e^-). This well explains the differences of catalytic activity of two spin states. Therefore, the catalytic activity of $C_2N–Co^{2+}$ may be regulated by adjusting the spin states, for which similar phenomenon is recently discovered on perovskite cobaltite electrocatalysts for oxygen evolution reaction.[49]

In order to elucidate the charge effect of Co^{2+} ion, we have examined the neutral state of $C_2N–Co$ (Figures 3 and S6). $C_2N–Co$ also has two spin states of S = 1/2 and 3/2. With the low spin state, the HCOOH dehydrogenation proceeds through three steps, which is similar to that on $C_2N–Co^{2+}$. The first H abstraction step occurs via transition state $TS_{9–10}$ with a barrier of 0.46 eV by reducing 0.25 eV energy. The products HCOO adsorbs on the surface via two Co–O bonds and one O–H hydrogen bond, and H adheres to the N atom. The second step is HCOO twisting motion via transition state $TS_{10–11}$. This process is endothermic by 0.30 eV, and needs to overcome a barrier of 0.49 eV. When HCOO locates at the bridge site through Co–O

and O–H hydrogen bonds, the second H abstraction step proceeds through transition state TS_{11-12} with a barrier of 0.88 eV and a reaction energy of 0.66 eV (endothermic reaction step). This means a high barrier of 0.66 eV for the rate-determining step of the overall reaction (Figure 3). While for the high spin state, the reaction process is analogous to that of the low spin state. The H abstraction takes place via TS_{13-14} with no barrier, which is endothermic by 0.06 eV. The formed HCOO twists through transition state TS_{14-15} with a barrier of 0.47 eV and a corresponding energy change of 0.03 eV (exothermic reaction step). In the end, the second H abstraction occurs via transition state TS_{15-16} with C–H bond scission, which is the rate-determining step with a high barrier of 0.93 eV (Table 2). Therefore, the HCOOH dehydrogenation catalyzed by neutral C_2N–Co (S =1/2 and 3/2) is difficult due to high barrier of rate-determining step (0.88 and 0.93 eV). In contrast, the low barrier of 0.30 eV for HCOOH dehydrogenation on C_2N–Co^{2+} (S = 1/2) suggests high catalyzing ability, Again, the NPA analysis (Table 1) revealed that Co^{2+} (S = 1/2) can extract 0.07 e^- electrons from HCOOH while that of neutral Co is very small (0.01 e^-).

We have also studied HCOOH dehydrogenation on C_2N–Cu^{2+} (S = 1/2) and C_2N–Ni^{2+} (S = 1). Once HCOOH adsorbs on the C_2N–Cu^{2+}, the H abstraction occurs via three elementary steps in Figure 4. The first O–H bond scission proceeds through transition state TS_{17-18}, where the breaking O–H bond is elongated to 1.34 Å from 1.03 Å. This process is endothermic with a reaction energy of 0.13 eV and a barrier of 0.10 eV. As the dissociated H atom moves to a N atop position, the newly formed HCOO binds to the surface through O–Cu and O–H hydrogen bonds. Then, the

HCOO twists through transition state TS_{18-19} with a barrier of 0.11 eV and a corresponding energy change of 0.05 eV (exothermic reaction step). The HCOO binds to the bridge site through O–Cu and O–H hydrogen bonds. In the end, the second H abstraction proceeds via transition state TS_{19-20} with a barrier of 0.85 eV, which is the rate-determining step of the overall reaction. The reaction steps catalyzed by $C_2N–Ni^{2+}$ (S = 1) were illustrated in Figure 5. Initially, HCOOH breaks its O–H bond via transition state TS_{21-22} with no barrier to form the HCOO intermediate, which is exothermic with a reaction energy of 0.34 eV. The H atom in the HCOO is ready to bind with the Ni^{2+} ion. The barrier for the twisting motion is 0.90 eV. Therefore, the barriers of the rate-determining steps of the HCOOH dehydrogenation on $C_2N–Cu^{2+}$ and $C_2N–Ni^{2+}$ are 0.88 eV and 0.90 eV, respectively, which is comparable with those catalyzed by noble Pt or Pd catalysts (0.65 ~ 0.88 eV).[45–47] After C–H bond scission, the formed CO_2 is weakly adsorbed to Cu^{2+} or Ni^{2+}, which can easily desorb with exothermic energy of 0.20 ~ 0.22 eV (Table 2).

4. Conclusions

In summary, we have studied HCOOH dehydrogenation catalyzed by $C_2N–TM^{x+}$ (Co^{2+}, Cu^{2+}, Ni^{2+}) using DFT calculations. We demonstrated that TM^{x+} ions bind strongly to two N atoms in C_2N, prohibiting the drifting of metal ions from one hole site to the neighboring hole site. Repulsion between two TM^{x+} ions forbids their aggregation, ensuring catalysis by a single-atom TM^{x+} site. It is revealed that the HCOOH dehydrogenation on $C_2N–TM^{x+}$ occurs through a dual-active centre (N and

TM^{x+}) with three elementary steps (O–H bond scission, HCOO twisting motion, and C–H bond scission). The computed energy barriers of the rate-determining step of the HCOOH dehydrogenation on the non-noble metal C$_2$N–Co^{2+} (S = 1/2), C$_2$N–Cu^{2+} and C$_2$N–Ni^{2+} sites are 0.30 ~ 0.90 eV, which is less than or comparable with those catalyzed by the noble metal Pt or Pd catalysts (0.65 ~ 0.88 eV). Different spin states (S = 1/2 and 3/2) of C$_2$N–Co^{2+} exhibit different catalytic ability in driving the HCOOH dehydrogenation due to variation in the ability to extract electrons. The catalytic activity of C$_2$N–Co^{2+} can thus be regulated by adjusting the spin states. The predicted excellent catalytic activity and reported mechanistic insights can lead to promising applications of low-cost, highly durable and highly efficient C$_2$N-supported single-atom transition metal ion catalysts for HCOOH dehydrogenation.

ASSOCIATED CONTENT

Supporting Information

Supplementary data related to this article can be found at http://dx.doi.org/ . Information of atomic structure, electron density, density of state, reaction potential profile of the C$_2$N-supported single-atom based transition metal ion catalysts are in Figures S1−S6.

Notes

The authors declare no competing financial interest.

REFERENCES

1 M. C. Orilall, F. Matsumoto, Q. Zhou, H. Sai, H. D. Abruna, F. J. DiSalvo, U. Wiesner, *J. Am. Chem. Soc.*, 2009, **131**, 9389–9395.

2 S. Uhm, H. J. Lee, J. Kwon, J. Lee, *Angew. Chem., Int. Ed.*, 2008, **47**, 10163–10166.

3 K.Tedsree, T. Li, S. Jones, C. W. A. Chan, K. M. K. Yu, P. A. J. Bagot, E. A. Marquis, G. D. W. Smith, S. C. E. Tsang, *Nat. Nanotechnol.*, 2011, **6**, 302–307.

4 Z. L. Wang, J. M. Yan, H. L. Wang, Y. Ping, Q. Jiang, *J. Mater. Chem. A*, 2013, **1**, 12721–12725.

5 Y. X. Chen, M. Heinen, Z. Jusys, R. J. Behm, *Angew. Chem., Int. Ed.*, 2006, **45**, 981–985.

6 D. Bin, B. B. Yang, F. F. Ren, K. Zhang, P. Yang, Y. K. Du, *J. Mater. Chem. A*, 2015, **3**, 14001–14006.

7 N. Tian, Z. Y. Zhou, S. G. Sun, Y. Ding, Z. L. Wang, *Science*, 2007, **316**, 732–735.

8 D. Chen, P. C. Sun, H. Liu, J. Yang, *J. Mater. Chem. A*, 2017, **5**, 4421–4429.

9 J. Mccarty, J. Falconer, R. J. Madix, *J. Catal.*, 1973, **30**, 235–249.

10 T. Fujitani, Y. Choi, M. Sano, Y. Kushida, J. Nakamura, *J. Phys. Chem. B*, 2000,

104, 1235–1240.

11　Q. Q. Luo, G. Feng, M. Beller, H. J. Jiao, *J. Phys. Chem. C*, 2012, **116**, 4149–4156.

12　V. Mazumder, M. F. Chi, M. N. Mankin, Y. Liu, O. Metin, D. H. Sun, K. L. More, S. H. Sun, *Nano Lett.*, 2012, **12**, 1102–1106.

13　M. A. Matin, J. H. Jang, Y. U. Kwon, *J. Power Sources*, 2014, **262**, 356–363.

14　D. E. Fein, I. E. Wachs, *J. Catal.*, 2002, **210**, 241–254.

15　J. Gong, H. J. Lin, M. Antonietti, J. Y. Yuan, *J. Mater. Chem. A*, 2016, **4**, 7313–7321.

16　X. Q. Lin, X. Z. Li, F. Li, Y. Y. Fang, M. Tian, X. C. An, Y. Fu, J. Jin, J. T. Ma, *J. Mater. Chem. A*, 2016, **4**, 6505–6512.

17　J. Mahmood, E. K. Lee, M. Jung, D. Shin, I. P. Jeon, S. M. Jung, H. J. Choi, J. M. Seo, S. Y. Bae, S. D. Sohn, *Nat. Commun.*, 2015, **6**, 6486–6492.

18　J. Mahmood, S. M. Jung, S. J. Kim, J. Park, J. W. Yoo, J. B. Baek, *Chem. Mater.*, 2015, **27**, 4860–4864.

19　X. F. Zhang, J. J. Guo, P. F. Guan, C. J. Liu, H. Huang, F. H. Xue, X. L. Dong, S. J. Pennycook, M. F. Chisholm, *Nat. Commun.*, 2013, **4**, 1924–1930.

20　B. T. Qiao, A. Q. Wang, X. F. Yang, L. F. Allard, Z. Jiang, Y. T. Cui, J. Y. Liu, J. Li, T. Zhang, *Nat. Chem.*, 2011, **3**, 634–641.

21　G. Kyriakou, M. B. Boucher, A. D. Jewell, E. A. Lewis, T. J. Lawton, A. E. Baber, H. L. Tierney, M. Flytzani-Stephanopoulos, E. C. H. Sykes, *Science*, 2012, **335**, 1209–1212.

22　X. Guo, G. Fang, G. Li, H. Ma, H. Fan, L. Yu, C. Ma, X. Wu, D. Deng, M. Wei, D. Tan, R. Si, S. Zhang, J. Li, L. Sun, Z. Tang, X. Pan, X. Bao, *Science*, 2014, **344**,

616–619.

23 X. Y. Li, W. H. Zhong, P. Cui, J. Li, J. Jiang, *J. Phys. Chem. Lett.*, 2016, **7**, 1750–1755.

24 M. Vázquez-González, W. C. Liao, R. Cazelles, S. Wang, X. Yu, V. Gutkin, I. Willner, *Nano Lett.*, 2017, **17**, 2043–2048.

25 M. Vázquez-González, W. C. Liao, R. Cazelles, S. Wang, X. Yu, V. Gutkin, I. Willner, *ACS Nano*, 2017, **11**, 3247–3253.

26 J. Wang, W. H. Zhong, X. Y. Liu, T. T. Yang, F. Li, Q. Li, W. R. Cheng, C. Gao, Z. Jiang, J. Jiang, H. Cui, *Anal. Chem.*, 2017, **89**, 13518–13523.

27 L. Nie, D. H. Mei, H. F. Xiong, B. Peng, Z. B. Ren, X. I. P. Hernandez, A. Delariva, M. Wang, M. H. Engelhard, L. Kovarik, A. K. Datye, Y. Wang, *Science*, 2017, **358**, 1419–1423.

28 D. A. Bulushev, M. Zacharska, E. V. Shlyakhova, A. L. Chuvilin, Y. N. Guo, S. Beloshapkin, A. V. Okotrub, L. G. Bulusheva, *ACS Catal.*, 2016, **6**, 681–691.

29 J. P. Perdew, K. Burke and M. Ernzerhof, *Phys. Rev. Lett.*, 1996, **77**, 3865–3868.

30 J. P. Perdew, S. Kurth, A. Zupan, P. Blaha, *Phys. Rev. Lett.*, 1999, **82**, 2544–2547.

31 X. Y. Li, P. Cui, W. H. Zhong, J. Li, X. J. Wang, Z. W. Wang, J. Jiang, *Chem. Commun.*, 2016, **52**, 13233–13236.

32 M. Mananghaya, *Int. J. Hydrogen Energy*, 2015, **40**, 9352–9358.

33 J. Andzelm, S. Huzinaga, *Gaussian Basis Sets for Molecular Calculations;* Elsevier Science: New York, 1984.

34 P. C. Hariharan, J. A. Pople, *Theor. Chim. Acta.*, 1973, **28**, 213–222.

35 K. Fukui, *J. Phys. Chem.*, 1970, **74**, 4161–4163.

36 K. Fukui, *Acc. Chem. Res.*, 1981, **14**, 363–368.

37 T. Lu, F. Chen, *J. Comput. Chem.*, 2012, **33**, 580–592.

38 F. Weinhold, C. R. Landis, E. D. Glendening, *Int. Rev. Phys. Chem.*, 2016, **35**, 399–440.

39 E. D. Glendening, C. R. Landis, F. Weinhold, *WIREs Comput. Mol. Sci.*, 2012, **2**, 1–42.

40 M. J. Frisch, G. W. Trucks, H. B. Schlegel, G. E. Scuseria, M. A. Robb, J. R. Cheeseman, G. Scalmani, V. Barone, B. Mennucci, G. A. Petersson, H. Nakatsuji, M. Caricato, X. Li, H. P. Hratchian, A. F. Izmaylov, J. Bloino, G. Zheng, J. L. Sonnenberg, M. Hada, M. Ehara, K. Toyota, R. Fukuda, J. Hasegawa, M. Ishida, T. Nakajima, Y. Honda, O. Kitao, H. Nakai, T. Vreven, J. A. J. Montgomery, J. E. Peralta, F. Ogliaro, M. Bearpark, J. J. Heyd, E. Brothers, K. N. Kudin, V. N. Starov-erov, T. Keith, R. Kobayashi, J. Normand, K. Raghavachari, A. Rendell, J. C. Burant, S. S. Iyengar, J. Tomasi, M. Cossi, N. Rega, J. M. Millam, M. Klene, J. E. Knox, J. B. Cross, V. Bakken, C. Adamo, J. Jaramillo, R. Gomperts, R. E. Stratmann, O. Yazyev, A. J. Austin, R. Cammi, C. Pomelli, J. W. Ochterski, R. L. Martin, K. Morokuma, V. G. Zakrzewski, G. A. Voth, P. Salvador, J. J. Dannenberg, S. Dapprich, A. D. Daniels, O. Farkas, J. B. Foresman, J. V. Ortiz, J. Cioslowski, D. J. Fox, *Gaussian 09,* Revision D.01; Gaussian, Inc.: Wallingford, CT, 2009.

41 O. Sato, J. Tao, Y. Z. Zhang, *Angew. Chem. Int. Ed.*, 2007, **46**, 2152–2187.

42 M. Bernien, H. Naggert, L. M. Arruda, L. Kipgen, F. Nickel, J. Miguel, C. F. Hermanns, A. Kruger, D. Kruger, E. Schierle, E. Weschke, F. Tuczek, W. Kuch, *ACS Nano*, 2015, **9**, 8960–8966.

43 Y. X. Liu, D. J. Zhang, J. Gao, C. B. Liu, *Chem. Eur. J.*, 2012, **18**, 15537–15545.

44 Y. Jiao, Y. Zheng, P. Chen, M. Jaroniec, S. Z. Qiao, *J. Am. Chem. Soc.*, 2017, **139**, 18093–18100.

45 M. Neurock, M. Janik, A. Wieckowski, *Faraday Discuss.*, 2008, **140**, 363–378.

46 W. Gao, J. A. Keith, J. Anton, T. Jacob, *J. Am. Chem. Soc.*, 2010, **132**, 18377–18385.

47 Y. Y. Wang, Y. Y. Qi, D. J. Zhang, C. B. Liu, *J. Phys. Chem. C*, 2014, **118**, 2067–2076.

48 J. Tomasi, B. Mennucci, R. Cammi, *Chem. Rev.*, 2005, **105**, 2999–3093.

49 Y. Tong, Y. Q. Guo, P. Z. Chen, H. F. Liu, M. X. Zhang, L. D. Zhang, W. S. Yan, W. S. Chu, C. Z. Wu, Y. Xie, *Chem*, 2017, 3, 812–821.

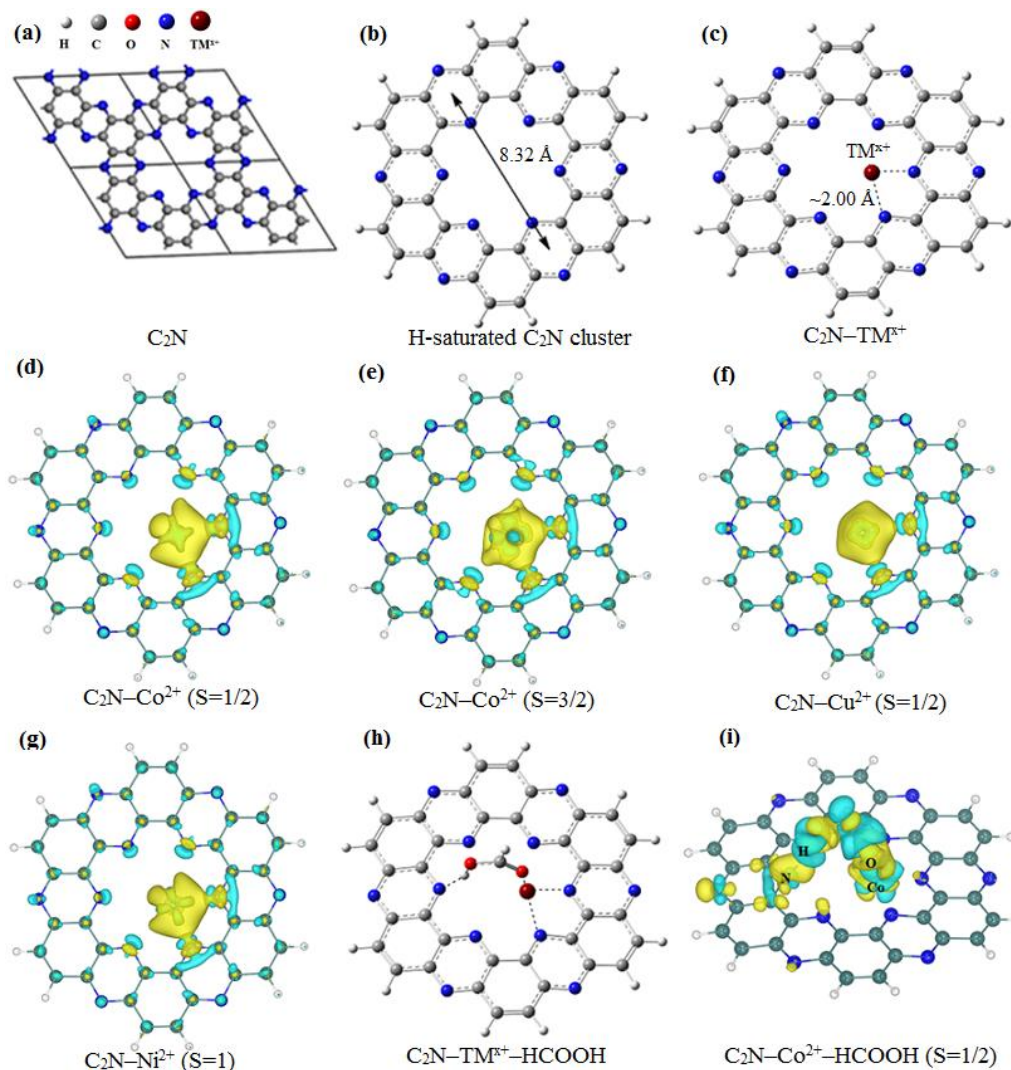**Figure 1**. **(a)** Atomic structure of the C_2N monolayer with the 2×2 supercell. **(b)** Structure of the H-saturated C_2N model cluster. **(c)** Structure of C_2N–TM^{x+} (TM^{x+} = transition metal ions). **(d)-(g)** Electron density difference for C_2N–TM^{x+} reflecting charge redistribution due to deposition of TM^{x+} on C_2N. The isosurface value is 0.006 e $Å^{-3}$. **(h)** Configuration of HCOOH adsorbed on C_2N–TM^{x+}. **(i)** Electron density difference for HCOOH adsorbed on C_2N–Co^{2+} ($S = 1/2$). The isosurface value is 0.002 e $Å^{-3}$. Yellow bubble represents electron accumulation and cyan bubble denotes electron depletion.

	$E_{b-TM^{x+}}$ (eV)	$E_{ads-HCOOH}$ (eV)	$C_2N \rightarrow TM^{x+}$ charge (e^-)	$HCOOH \rightarrow C_2N-TM^{x+}$ charge (e^-)
$C_2N-Co^{2+}(S=1/2)$	15.16	0.83	−1.11	−0.07
$C_2N-Co^{2+}(S=3/2)$	14.34	0.84	−0.96	−0.04
$C_2N-Co(S=1/2)$	3.09	0.49	0.77	0.01
$C_2N-Co(S=3/2)$	2.67	0.58	0.82	−0.04
$C_2N-Cu^{2+}(S=1/2)$	16.14	0.48	−1.12	−0.02
$C_2N-Ni^{2+}(S=1)$	14.64	1.15	−1.08	0.01

Table 1. Computed binding energies of TM^{x+} on C_2N, adsorption energies of the HCOOH molecule on C_2N-TM^{x+}, charges extracted from C_2N to TM^{x+} ($C_2N \rightarrow TM^{x+}$) in the hybrid systems, and charges extracted from HCOOH to C_2N-TM^{x+} in the adsorption configuration.
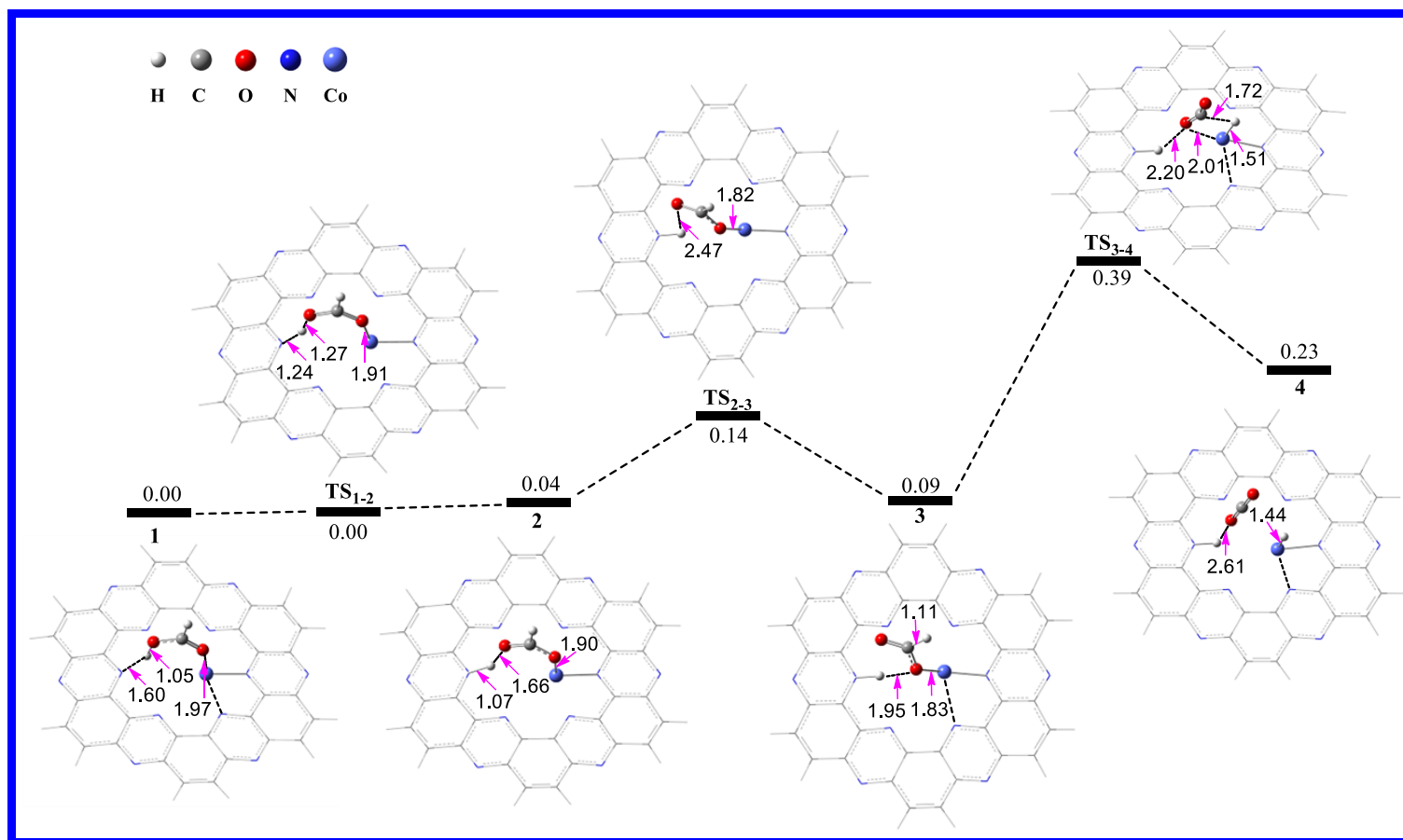
Figure 2. Calculated potential energy profile of the HCOOH dehydrogenation reaction on $C_2N–Co^{2+}$ (S = 1/2) with the optimized geometries of intermediates and transition states involved in the reaction. The relative free energies are given in eV. The distances are in Å.
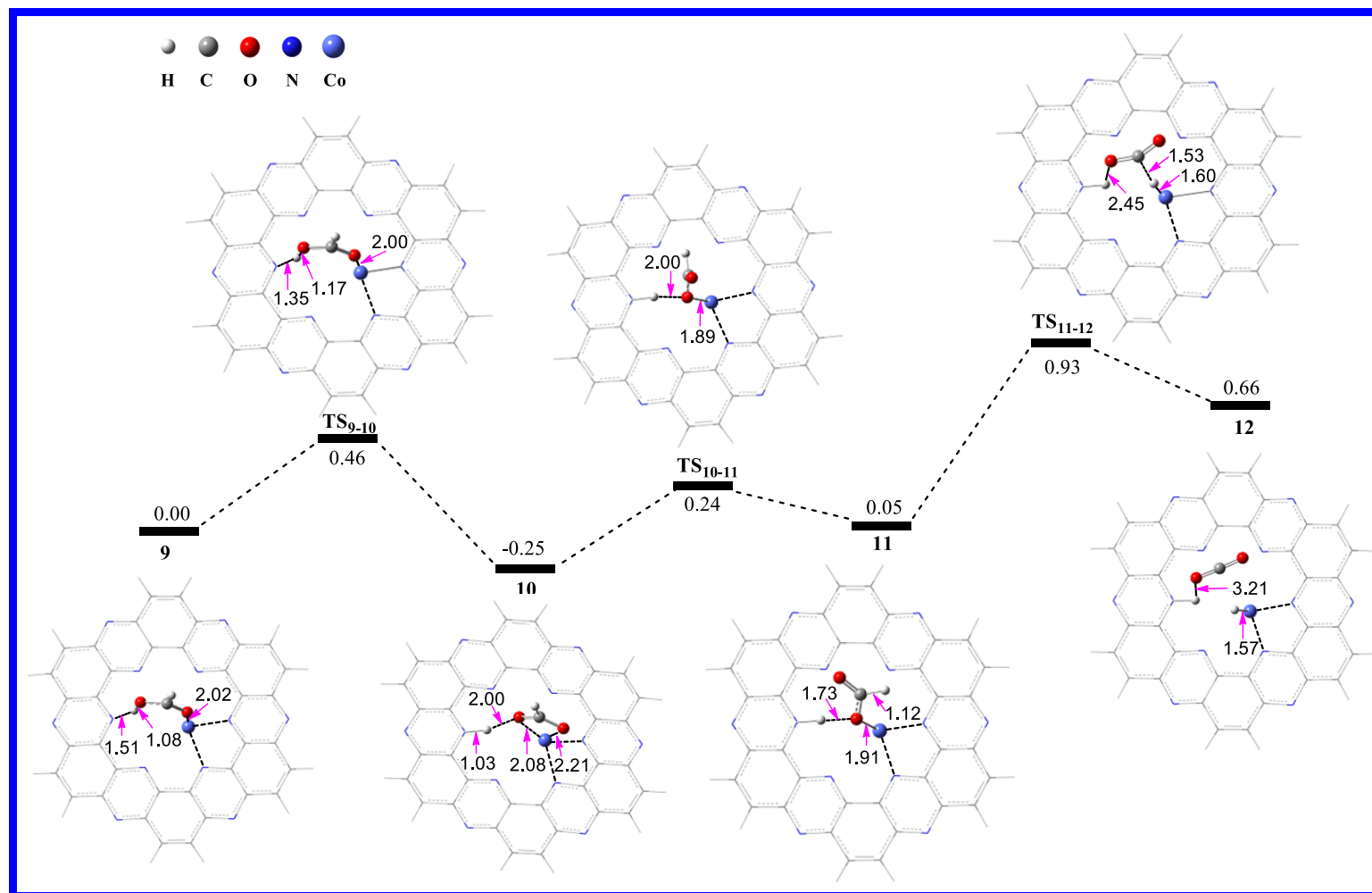
Figure 3. Calculated potential energy profile of the HCOOH dehydrogenation reaction on C_2N–Co ($S = 1/2$) with the optimized geometries of intermediates and transition states involved in the reaction. The relative free energies are given in eV. The distances are in Å.
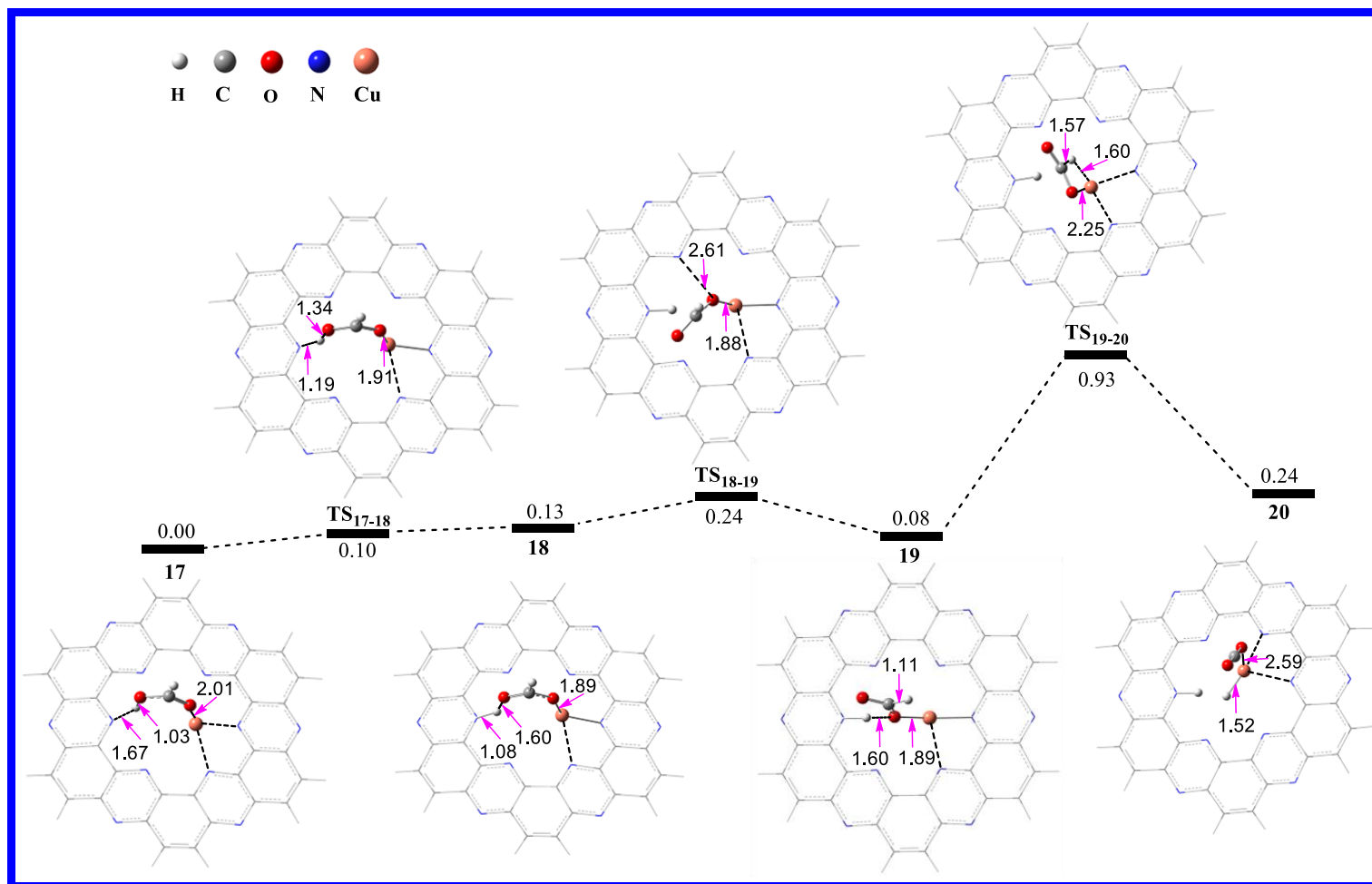
Figure 4. Calculated potential energy profile of the HCOOH dehydrogenation reaction on $C_2N–Cu^{2+}$ (S = 1/2) with the optimized geometries of intermediates and transition states involved in the reaction. The relative free energies are given in eV. The distances are in Å.
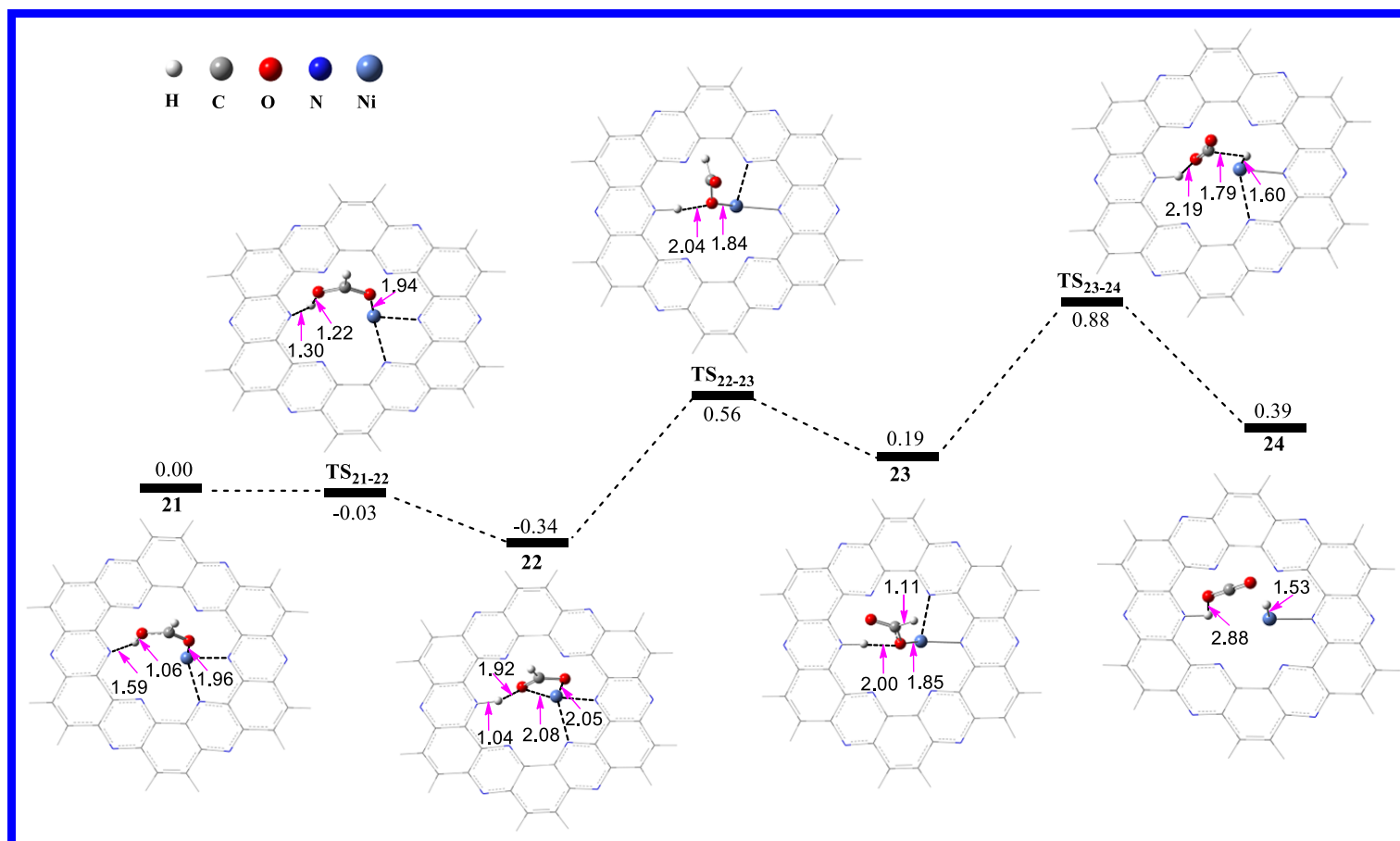
Figure 5. Calculated potential energy profile of the HCOOH dehydrogenation reaction on $C_2N–Ni^{2+}$ (S = 1) with the optimized geometries of intermediates and transition states involved in the reaction. The relative free energies are given in eV. The distances are in Å.

	E_a(TS1)	E_a(TS2)	E_a(TS3)	O–H(TS1)	TM^{x+}–O(TS2)	C–H(TS3)	CO_2 desorption
C_2N–Co^{2+}(S=1/2)	0.00	0.10	0.30	1.27	1.82	1.72	– 0.23
C_2N–Co^{2+}(S=3/2)	–0.02	0.24	1.05	1.23	1.83	1.87	– 0.54
C_2N–Co(S=1/2)	0.46	0.49	0.88	1.17	1.89	1.53	– 0.30
C_2N–Co(S=3/2)	–0.04	0.47	0.93	1.17	1.89	1.49	– 0.30
C_2N–Cu^{2+}(S=1/2)	0.10	0.11	0.88	1.34	1.88	1.57	– 0.20
C_2N–Ni^{2+}(S=1)	–0.03	0.90	0.69	1.22	1.84	1.79	– 0.22

Table 2. Calculated energy barrier (eV), O–H, TM^{x+}–O and C–H bond lengths (Å), and CO_2 desorption energy (eV) of the HCOOH dehydrogenation reaction catalyzed by C_2N–TM^{x+}. $E_{CO2–desoption} = E_{CO2} + E_{C2N–TM^{x+}–2H} − E_{C2N–TM^{x+}–CO2–2H}$.

SYNOPSIS TOC
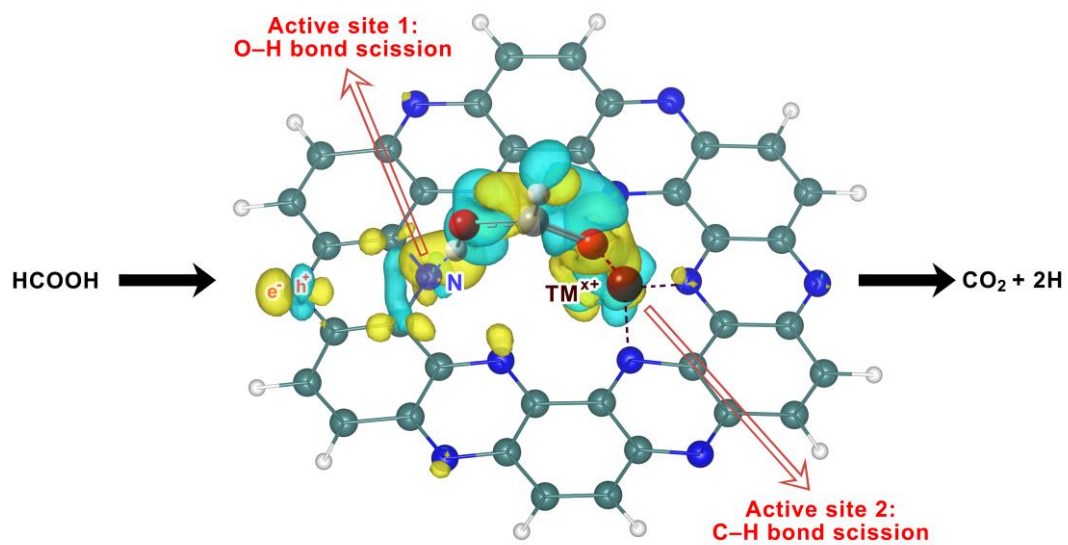
Polarized charges on dual-reactive centers of C_2N-supported single-atom based transition metal ion catalyst promoting HCOOH dehydrogenation.